

Enhancing Spatial Resolution of Hyperspectral Imagery Using Sensor's Intrinsic Keystone Distortion

Shen-En Qian, *Senior Member, IEEE*, and Guangyi Chen

Abstract—In this paper, we develop a novel technology that can enhance the spatial resolution of hyperspectral data cube without using any additional images, as would be the case in image fusion. The technology exploits interband spatial misregistration or distortion (often referred to as “keystone”) of the sensor that acquired the data cube and uses it as additional information to increase the spatial resolution of the data cube. Three methods have been developed to derive subpixel-shifted images from the data cube itself in exploiting the sensor's intrinsic characteristics. Two schemes were proposed to organize the derived subpixel-shifted images before being integrated into the high-resolution image using the iterative-back-projection fusion. Experimental results show that the technology can enhance the spatial resolution in the cross-track direction of hyperspectral data cubes by a factor of two.

Index Terms—Enhancing spatial resolution, hyperspectral sensors, image fusion, image processing, sensor's spatial distortion (keystone).

I. INTRODUCTION

SPATIAL resolution, also referred to as ground sample distance (GSD), is one of the key parameters in design and building of an imaging satellite sensor. Satellite data users always prefer to receive images with high spatial resolution in order to better serve their applications. Designing and building a satellite sensor with a considerably high spatial resolution is one of the challenges, as this could be prohibitively expensive and/or constrained by technology availability. For example, Phase A study of the Canadian Hyperspectral Environment and Resource Observer mission concluded that the achievable GSD is 30 m. This GSD comes out as the engineering tradeoff between spectral and spatial resolutions in the sensor design as a result of the need to maintain imaging sensitivity at the finer spectral resolution [1]. However, users prefer and/or require even higher GSD (e.g., 20 or 10 m).

To increase the spatial resolution of satellite images, image fusion is nominally an alternative solution. Multiple images of the same scene observed by the same sensor at different times or observed by different sensors at either the same time or different times are fused to attain a high-spatial-resolution image [2]. In

the case of multispectral or hyperspectral sensors, the spatial resolution of multispectral or hyperspectral imageries can be enhanced by fusing the low-resolution (LR) multispectral or hyperspectral imageries with a high-spatial-resolution panchromatic (PAN) image that was acquired simultaneously by the PAN instrument on board the same satellite. However, the image-fusion-based spatial-resolution-enhancement approach requires multiple observed images of the same scene or the high-spatial-resolution PAN image being available. In real practices, these images may not be always available. Even if the multiple images of the same scene or high-spatial-resolution PAN image is available, it is a nontrivial task to fuse the images to precisely enhance the spatial resolution.

An accurate geometric registration and the radiometric normalization of the images to be fused are crucial, since the multiple images of the same scene acquired by different sensors or by the same sensor at different times are inconsistent [3]. They are not at a common geometric base and a common radiometric base. Without a common geometric base, the multiple images of the same scene are not associated with each other for the spatial information. This makes precise spatial-resolution enhancement difficult. The fidelity of the fused images is dependent on the accurate registration of the multiple images to a common spatial framework [4], [5].

Without a common radiometric base, it is difficult to fuse the multiple images of the same scene that were acquired at different illumination and atmospheric conditions, view angles, or sensor parameters, because these variations cause the pixel intensity difference in the images, while this difference does not reflect the actual object difference in the scene. The multiple images of the same scene need to be well normalized to a common radiometric framework. Inaccurate radiometric normalization of the multiple images of the same scene severely compromises the quality of the fused image.

Motivated by the demand on higher spatial resolution of acquired satellite images and the constraints and technical difficulties to enhance spatial resolution of the images using the conventional fusion approach, a novel technology for enhancing spatial resolution of satellite imageries based on the imaging sensor's characteristic has been developed at the Canadian Space Agency. This technology can enhance the spatial resolution of acquired imageries without using any additional images, as would be the case in image fusion. It exploits the intrinsic characteristic of hyperspectral sensors, i.e., interband spatial misregistration or distortion often referred to as

Manuscript received May 7, 2011; revised August 2, 2011, October 26, 2011, and December 19, 2011; accepted April 1, 2012. Date of publication May 24, 2012; date of current version November 22, 2012.

The authors are with the Canadian Space Agency, Saint-Hubert, QC J3Y 8Y9, Canada.

Color versions of one or more of the figures in this paper are available online at <http://ieeexplore.ieee.org>.

Digital Object Identifier 10.1109/TGRS.2012.2195666

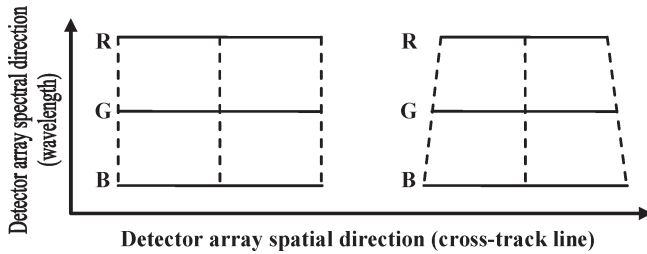


Fig. 1. Schematic of spatial distortion (KS) of a push-broom imaging spectrometer. On the left, the lines for blue (B), green (G), and red (R) are all straight, parallel, and aligned with the detector array. On the right, the lines G and R are shorter than line B because of KS. The amount of KS is measured by the difference in lengths between the lines B and R.

“keystone” (KS), and uses it as additional information to increase the spatial resolution of the imageries. Since multiple images of the same scene are no longer required, the enhancement of spatial resolution is irrespective of the registration and the radiometric normalization of the images.

This paper is organized as follows. Section II describes what KS is in hyperspectral sensors and how it can be exploited as additional information for enhancing spatial resolution. After a brief literature view on fusion of subpixel-shifted images, Section III proposes three methods for deriving subpixel-shifted images from a hyperspectral data cube itself by exploiting the KS characteristic and two schemes of organizing the derived subpixel-shifted images in order to obtain a single-band high-resolution (HR) image. Section IV shows the experimental results of single-band HR images obtained using the methods proposed in Section III. Section V describes how to enhance the spatial resolution of an entire data cube using the single-band HR image. Section VI reports the experimental results of the data cubes after spatial-resolution enhancement using performance metrics. Finally, Section VII draws the conclusion.

II. KEYSTONE—SENSOR’S INTRINSIC CHARACTERISTIC

A push-broom imaging spectrometer employs a 2-D detector array. The spectrum is dispersed in one dimension, for example, along the columns of the detector array, and the spatial field is oriented along the rows of the detector array. Ideally, this type of imaging spectrometer generates 2-D (spectral–spatial) frames of data in which all the entries in a given column image the same ground sample, as shown in the left graphics of Fig. 1. Due to geometric distortion, as can be seen in camera lenses, chromatic aberration, or a combination of both, interband spatial misregistration occurs, as shown in the right graphics of Fig. 1. This spatial distortion or misregistration is often called KS. It refers to the across-track spatial misregistration of the ground sample pixels of the various spectral bands of the spectrograph. Because the detector elements are arranged on a rectilinear grid, the presence of KS prevents the registration of a given ground sample pixel onto the elements of a single column in the detector array. Instead, a particular spatial pixel number in one spectral band, corresponding to a specific detector element number in the across-track dimension, will not be registered on the ground sample pixel with the corresponding pixel number in the other spectral bands. This means that, if two

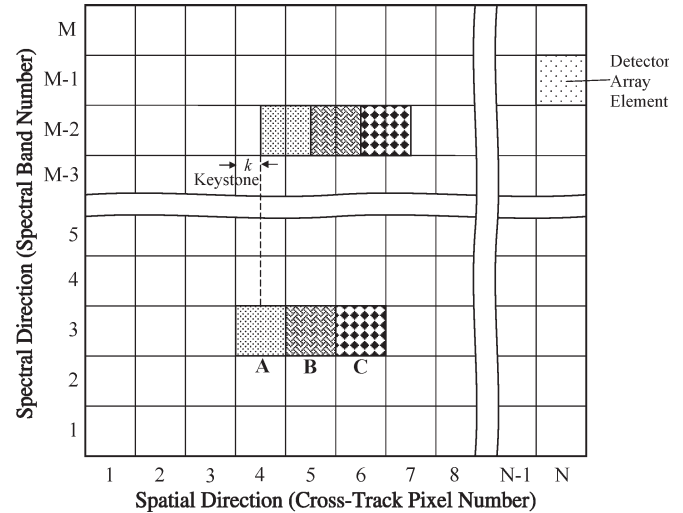


Fig. 2. Illustration of spatial shift of (A, B, and C) ground sample pixels imaged in detector array varying with spectral-band number or wavelength caused by KS.

neighboring ground samples are different targets (e.g., A and B in Fig. 2), with different spectra, then the spectrum measured by the sensor will be a mixture of the spectra of the two different target materials in which the fractional content of each material, and each spectrum, will vary with band number or wavelength.

KS occurs in every push-broom imaging spectrometer, even if a whisk-broom imaging spectrometer still exhibits certain amount of KS [6]. KS makes it difficult to identify material species in a spatially variable scene from the acquired imageries. A KS figure is a key parameter in designing and building an imaging spectrometer. Designing and building an imaging spectrometer with considerably small KS is one of the struggling goals in the development of the instrument [1]. For acquired imageries, the KS distortion of the imageries needs to be sufficiently corrected before the imageries are applied to derive productive information in order to reduce the effect of KS on the applications [7].

In contradiction to the negative impact of KS, the KS effect makes targets on the ground be imaged in detector array with spatial shift varying with spectral-band number or wavelength. For example, ground pixels A, B, and C imaged in band M-2, as shown in Fig. 2, are shifted by k -pixel compared to those imaged in band 3 due to KS distortion. This KS-induced spatial shift of the same ground sample pixels in different band images is additional information. It carries similar spatial information as multiple observations of the same scene. If this spatial information is well exploited, it can be utilized to enhance the spatial resolution of the imageries.

The KS amount varies with spatial locations and spectral bands in a detector array. The overall KS amount of an imaging spectrometer is a combination of the so-called “classic” KS and rotational misalignment of the instrument. Neville *et al.* have developed a method to detect the KS amount of an imaging spectrometer using an image data set acquired by the instrument based on the interband correlation of spatial features in the scene [6]. Fig. 3 shows two contour plots of spatial shift of band images relative to a reference band image. The left graphics shows the contour plot of spatial shifts of the Aurora

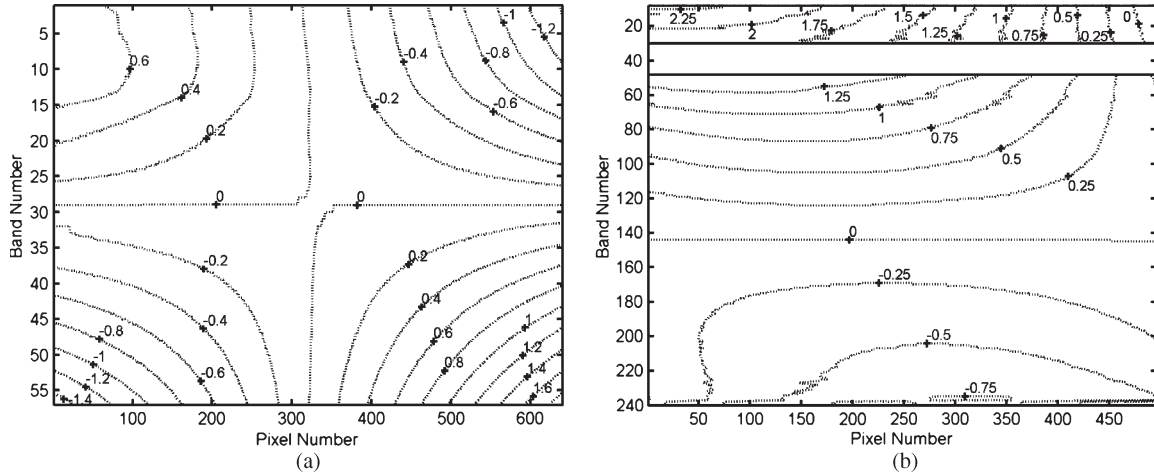


Fig. 3. Contour plots of spatial shift caused by KS of (a) Aurora sensor (relative to reference band image 29) and (b) SFSI sensor (relative to reference band image 144) [6].

sensor relative to the reference band image 29 of the sensor. Aurora is a 640-pixel-by-57-spectral-band airborne imaging spectrometer which covers the visible and near-infrared spectral range (394.50–933.22 nm). A positive value is to the right shift, and a negative value is to the left shift. The shift values in the upper left quadrant of the contour plot are positive, indicating that these pixels are shifted to the right by amounts which are proportional to their distance from the vertical and horizontal center lines of the array. The shift values in the upper right quadrant are negative, indicating that these pixels are shifted to the left. The overall symmetry of the contour lines and the fact that the zero-shift contour aligns quite well with the center across-track pixel are indicative of the precision of the optomechanical alignment of the instrument. This indicates that the spatial misregistration is attributed almost exclusively to the classic KS. The maximum and minimum spatial shifts relative to the reference band image are 1.91 and -1.51 pixels, respectively, for an overall maximum shift of 3.42 pixels.

The right graphics depicts the contour plot of spatial shifts relative to the reference band image (144) of the Short-wave infrared (SWIR) Full Spectrum Imager (SFSI) [8]. The SFSI is a push-broom imaging spectrometer with 496 pixels across track and 240 spectral bands covering a SWIR spectral range of 1217.3–2427.9 nm. Band images 30–48 are blanked out in the plot due to the strong water-vapor atmospheric absorption region (~ 1400 nm) where the sensor signal approaches zero. The detection method produced inconsistent results across this region. The maximum and minimum spatial shifts relative to the reference band image are 2.31 and -0.78 pixels, respectively, for a total span of 3.09 pixels. The corresponding mean rms KS measure is 0.598 pixels. The measured KS results indicate that the upper half of the SFSI instrument rotates to the right and the lower half rotates to the left.

III. USING KEYSTONE TO INCREASE SPATIAL RESOLUTION OF A SINGLE-BAND IMAGE

This section describes how to exploit the additional information hidden in the spatially shifted images of different band images induced by KS distortion and how to utilize it

to increase the spatial resolution of a single-band image. The spectral distortion (also referred to as smile) of a hyperspectral sensor exists in conjunction with the KS distortion. However, it is not considered in the present work due to its spectral distortion nature.

A. Fusion of Subpixel-Shifted Images

Image fusion methods have been developed to reconstruct an HR image by fusing subpixel-shifted LR images of the same scene. These methods can be generally categorized into five approaches: nonuniform interpolation, frequency-domain reconstruction, regularized reconstruction, projection onto convex sets, and iterative back projection (IBP) [10]. The nonuniform interpolation approach fuses the LR images by first estimating relative motion of the images, then nonuniformly interpolating the images onto HR grid to produce an HR resolution image, and finally deblurring the HR image based on the observation model [11]–[13]. The frequency-domain approach reconstructs an HR image based on the relationship between LR images and a desired HR image resulting from the relative motion between the LR images and the aliasing existing in each LR image [14]. The regularized approach includes constrained least squares and maximum *a posteriori* (MAP) HR image reconstruction methods according to the procedures adopted to stabilize the inversion of ill-posed problem because of an insufficient number of LR images and ill-conditioned blur operators [15]–[19]. The projection onto convex sets is an iterative approach to incorporating prior knowledge on the solution into the reconstruction process. With the estimates of registration parameters, this method simultaneously solves the restoration and interpolation problem to estimate the HR image [20], [21]. The IBP approach iteratively uses the current best estimated HR image to create the simulated LR images and then compare the simulated LR images to the observed LR images to create the difference images. These difference images are then used to improve the initial estimation by “back projecting” each value in the difference image onto the HR image [22], [23].

In this paper, the IBP image fusion approach is adopted to integrate the images with subpixel shift derived by exploiting

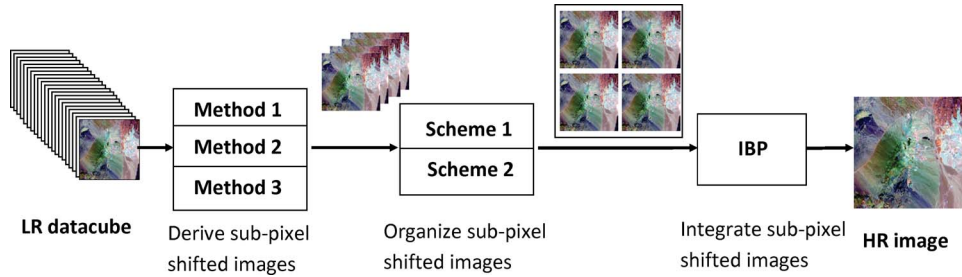


Fig. 4. Block diagram of generating the single-band HR image by exploiting the KS.

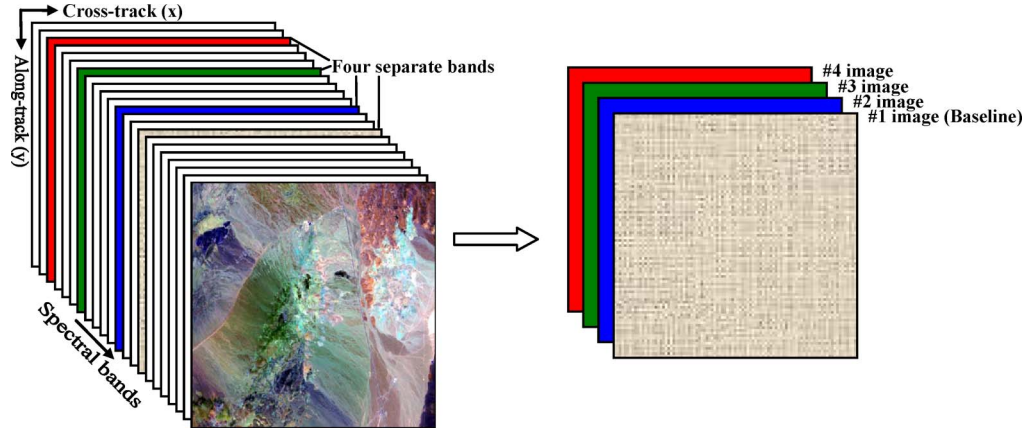


Fig. 5. Four spectral-band images extracted from a data cube to be enhanced based on KS-induced subpixel shift related to the baseline image.

the KS characteristics to produce a single-band HR image. This is because the IBP approach does not have constraint on motion of the multiple images and allows arbitrary motion such as translation, rotation, and scaling. It converges quickly and allows including other fast convergence methods. It is not computationally complex. IBP only deals with simple projection operation so that it can meet the need of real-time processing. It also includes iterative deconvolution. IBP can be regarded as an iteratively deblurring operation. It is not necessary to do the prefiltering and postfiltering operations that have to be done to compensate high-frequency components in other approaches.

Without loss of generality, let us see how a factor of two of spatial-resolution enhancement can be obtained using the subpixel-shifted images derived by exploiting the KS characteristics. To produce an HR image with a factor of two, $2 \times 2 = 4$ subpixel-shifted LR images are required. In this paper, three methods have been proposed to derive the four subpixel-shifted images from a hyperspectral data cube itself by exploiting the KS characteristics. This section describes these three methods and two proposed schemes of organizing the derived subpixel-shifted images before being integrated using IBP to generate the single-band HR image. Fig. 4 shows a block diagram of generating the single-band HR image by exploiting the KS characteristics.

B. Method 1—Separate Band Images Extracted Based on KS-Induced Subpixel Shift

A band image is first selected and extracted from a data cube to be enhanced for GSD and is taken as the reference

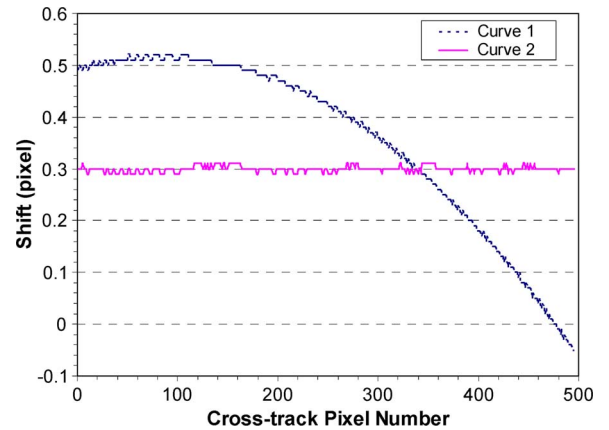


Fig. 6. Pixel shift as a function of pixel location in cross-track direction. (Curve 1) Between a baseline image and a selected band image. (Curve 2) Between a baseline image and a derived image using Method 2 in exploiting the KS characteristics.

for relating subpixel shifts to other band images. This image is referred to as the baseline image in this paper. Three band images then are selected and extracted from the data cube according to the required KS-induced subpixel shift between the baseline image and the selected band images. This method is shown in Fig. 5. These images are normally picked up from a spectral region with relative high spectrum amplitudes and a flat spectrum variation in order to reduce the impact of noise and spectrum variation between the images. For spatial-resolution enhancement with a factor of two, a 1/2-pixel shift between the images is ideal. With this shift, the LR pixels are all located on the HR grid and do not need to be interpolated [10]. Normally,

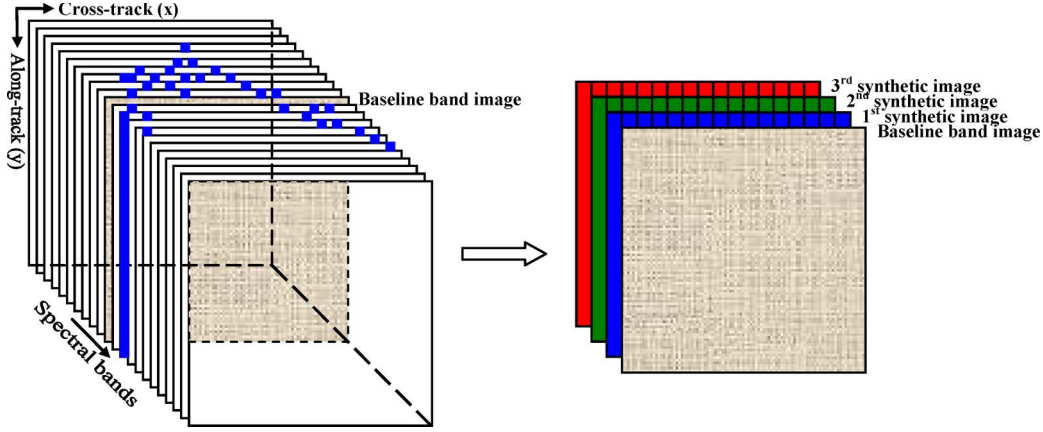


Fig. 7. Baseline image and three synthetic images derived by picking up columns from different band images based on a given amount pixel shift (in the figure, only the selected columns for the first synthetic image are shown).

spatial shifts of the pixels between the baseline image and a selected band image are not the same. This is because the KS amounts of the pixels of a band image vary across the spatial direction in the detector array, as shown in Fig. 3. Owing to the nature of successive approximation in the iteration of the IBP fusion method, any subpixel shift will contribute to the enhancement of spatial resolution. Fig. 6 shows an example of pixel shifts between the baseline band image and an extracted band image (Curve 1). It can be seen from the figure that the spatial shifts between the two images are between -0.05 and 0.52 pixels.

The dynamic range of pixel intensities of the extracted images may be different, since the images are apart spectrally. It is necessary to normalize them in order to reduce the impact of the intensity variations. In this paper, the mean and standard deviation of each of the extracted images are normalized to those of the baseline image. Assuming that the mean and standard deviation of the baseline image are μ_b and σ_b

$$\mu_b = \frac{1}{NM} \sum_{j=1}^N \sum_{i=1}^M p_b(i, j) \quad (1)$$

$$\sigma_b = \left(\frac{1}{NM} \sum_{j=1}^N \sum_{i=1}^M [p_b(i, j) - \mu_b]^2 \right)^{\frac{1}{2}} \quad (2)$$

where $p_b(i, j)$ is the intensity of pixel (i, j) of the baseline image and M and N are the total numbers of columns and rows of the image, respectively. The mean of a selected image is μ_k

$$\mu_k = \frac{1}{NM} \sum_{j=1}^N \sum_{i=1}^M p_k(i, j) \quad (3)$$

where $p_k(i, j)$ is the intensity of pixel (i, j) of the selected image. First, the mean of the selected image is removed from the image

$$p_{k-m}(i, j) = p_k(i, j) - \mu_k, \quad i = 1, 2, 3, \dots, M; \quad j = 1, 2, 3, \dots, N. \quad (4)$$

Then, the standard deviation of the selected image after mean removal is calculated

$$\sigma_{k-m} = \left(\frac{1}{NM} \sum_{j=1}^N \sum_{i=1}^M p_{k-m}(i, j)^2 \right)^{\frac{1}{2}}. \quad (5)$$

Finally, the image is normalized by multiplying σ_b/σ_{k-m} and adding μ_b

$$p_{k-norm}(i, j) = p_{k-m}(i, j) \frac{\sigma_b}{\sigma_{k-m}} + \mu_b, \quad i = 1, 2, 3, \dots, M; \quad j = 1, 2, 3, \dots, N. \quad (6)$$

C. Method 2—Synthetic Images Derived Based on a Given Amount of Subpixel Shift

A band image is first selected and extracted from a data cube to be enhanced and is taken as the baseline image, as in Method 1. Each of the other three synthetic images is then derived by picking up columns that have the required amount of pixel shift related to the baseline image, on a column-by-column basis, from the band images of the data cube. Fig. 7 shows this method. A synthetic image is composed of the columns that are extracted from different band images and have the same predefined amount of pixel shift related to the baseline image. Curve 2 in Fig. 6 shows the pixel shifts between a derived image and the baseline image with a predefined pixel shift of 0.3 . It can be seen that pixel shifts are close to the predefined value of 0.3 .

The dynamic range of the column of pixels that are picked up from a band image may be different from that of the same column of pixels of the baseline image, since these two columns of pixels are apart spectrally. It is necessary to normalize them in order to reduce the impact of the intensity variations. In this paper, the mean and standard deviation of each of the extracted columns are normalized to those of the same column of the baseline image. The normalization procedure is the same as that described in Section III-B.

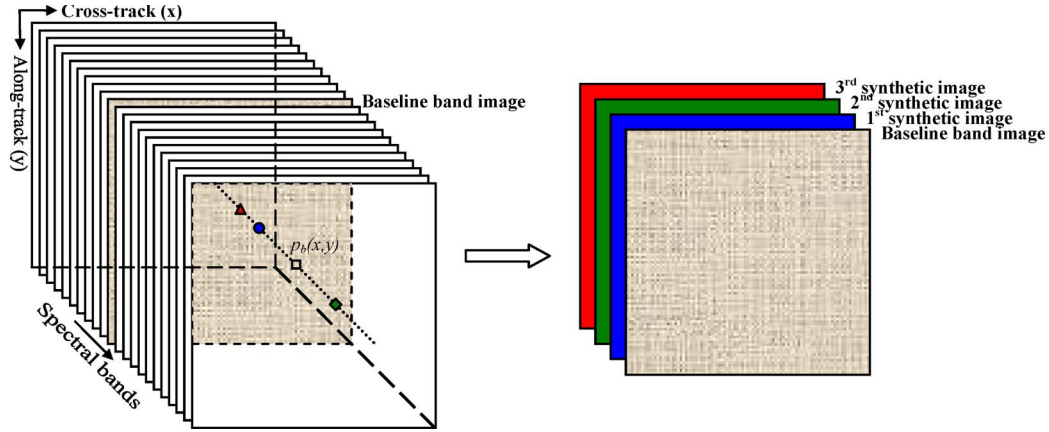


Fig. 8. Baseline image and three synthetic images derived by finding the pixel with the closest intensity to each of the pixels of the baseline image across the spectral bands [pixel circle is the first, pixel diamond is the second, and pixel triangle is the third closest to pixel $p_b(x, y)$].

D. Method 3—Synthetic Images Derived Based on Closeness of Pixel Intensity

A band image is first selected and extracted from a data cube to be enhanced and is taken as the baseline image. Each of the other three synthetic images is then derived by looking for the closest intensity to pixel $p_b(x, y)$ ($x = 1, 2, 3, \dots, M$; $y = 1, 2, 3, \dots, N$) of the baseline image in all the spectral bands. The first synthetic image is composed by the pixels found across the spectral bands that have the closest intensity to the pixels at the same location in the baseline image. The second synthetic image is composed by the pixels found across the spectral bands that have the second closest intensity to the pixels at the same location in the baseline image. The third synthetic image is composed by the pixels that have the third closest intensity to the pixels at the same location in the baseline image. This method is shown in Fig. 8. The intensities of the pixels in the three synthetic images derived in this way are close to those of the baseline image. Thus, their dynamic range of pixel intensities does not need to be adjusted. Pixel shifts between a synthetic image and the baseline image vary in both cross- and along-track directions. Fig. 9 shows the plane of pixel shifts between a synthetic image and the baseline image as a function of 2-D spatial locations.

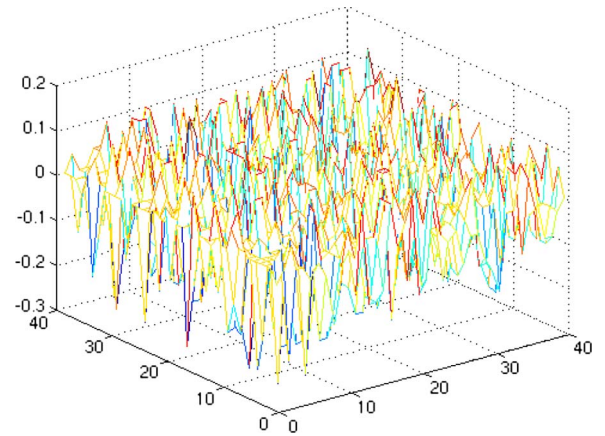


Fig. 9. Plane of pixel shift between the baseline image and a synthetic image derived based on the closeness of pixel intensity. The amount of spatial shift (vertical axis in pixel) of the pixels varies as a function of pixel location in both cross-track (x) and along-track (y) directions.

E. Two Schemes of Organizing Subpixel-Shifted Images and IBP Implementation

For a factor-of-two increase of spatial resolution, four images of the same scene having 1/2-pixel shift in both two dimensions are required, as shown in Fig. 10. The four subpixel-shifted images derived using the three methods described earlier need to be arranged and organized before being integrated. It is known that the spatial shift between the band images of a hyperspectral data cube induced by KS is only in the cross-track direction. The spatial shifts of the pixels in an image derived using the aforementioned three methods in the cross-track direction related to the baseline image are variable and not always equal to 1/2 pixel. Two schemes are proposed to organize the four derived LR images before being input to IBP as I_{00} , I_{10} , I_{01} , and I_{11} for creating the HR image and shown in Fig. 11.

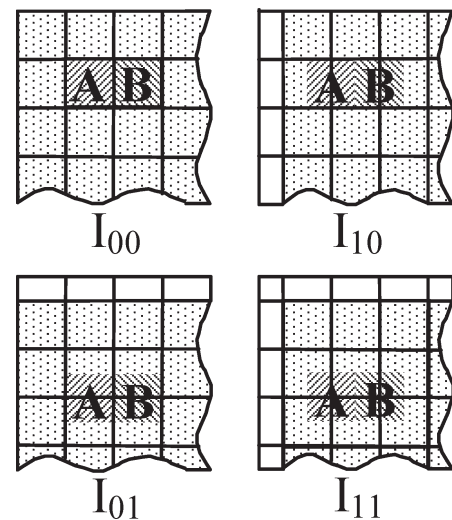


Fig. 10. Four multiple observation images with subpixel shifted to be input to IBP for fusion. I_{10} is 1/2-pixel right shift to I_{00} , I_{01} is 1/2-pixel down shift to I_{00} , and I_{11} is 1/2-pixel both right and down shift to I_{00} .

In Scheme 1, the baseline image is taken as I_{00} . The KS-induced pixel shifts in one of the images derived using the methods earlier are uniformly resampled to 1/2-pixel right shift

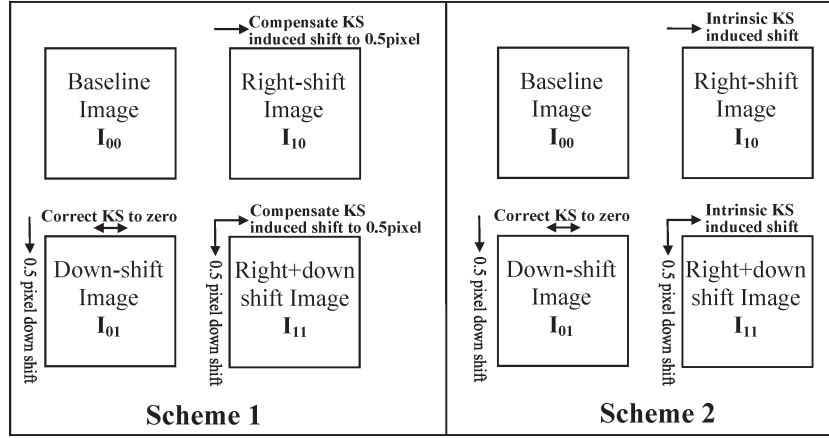


Fig. 11. Two schemes of organizing the derived subpixel-shifted images into I_{00} , I_{10} , I_{01} , and I_{11} .

by compensating the existing shifts. This resampled image is taken as I_{10} . Another derived image is corrected to zero KS shift related to the baseline image to align it with the baseline image in the cross-track direction. Then, this KS-corrected image is shifted 1/2 pixel down (along track) and is taken as I_{01} . I_{11} is assigned by resampling the third derived image to 1/2 pixel right by compensating the existing shifts and down shift related to the baseline image.

In Scheme 2, the four derived images are organized similarly as in Scheme 1, except that I_{10} and I_{11} are not resampled to 1/2-pixel right shift by compensating the existing shifts. They remain the intrinsic KS pixel shifts related to the baseline image. In Scheme 2, due to the KS-induced pixel shifts not being uniformly resampled to 1/2 pixel, it is important to assign a derived image with close to 1/2-pixel KS-induced shift as I_{10} or I_{11} and assign a derived image with close to zero KS-induced shift as I_{01} .

The IBP algorithm consists of two steps—*projection* and *back projection*. It performs these two steps iteratively until satisfactory results are obtained. It starts to approximate the HR image using an initial estimation HR image $f^{(0)}$ and simulates the imaging process using a blurring function h_k and a down-sampling operator $\downarrow s$ to generate a set of LR images $\{g_k^{(0)}\}$. If $f^{(0)}$ is equal to the real HR image (which is unknown), then the simulated LR images $\{g_k^{(0)}\}$ should be identical to the observed images $\{g_k\}$. Otherwise, the initial estimation HR image $f^{(0)}$ is updated using the difference images $\{g_k - g_k^{(0)}\}$ to generate an improved HR image $f^{(1)}$. This process is repeated until the minimum error between the simulated LR images and observed images is reached

$$e^{(n)} = \left[\frac{1}{K} \sum_{k=1}^K \left(g_k - g_k^{(n)} \right)^2 \right]^{1/2} \quad (7)$$

where $g_k^{(n)}$ is the simulated LR image k in the n th iteration and K is the total number of the LR images. The simulated LR images $\{g_k^{(n)}\}$ are obtained by

$$g_k^{(n)} = \left(T_k(f^{(n)}) * h_k \right) \downarrow s \quad (8)$$

where T_k is a 2-D geometric transformation from f to g_k , $*$ is the convolution operator, and $\downarrow s$ denotes a down-sampling operator by a factor of s . The update of the HR image is given by

$$f^{(n+1)} = f^{(n)} + \frac{1}{K} \sum_{k=1}^K T_k^{-1} \left\{ \left[\left(g_k - g_k^{(n)} \right) \uparrow s \right] * p \right\} \quad (9)$$

where $\uparrow s$ is an up-sampling operator by a factor of s and p is a back-projection kernel, which is determined by h_k and T_k .

In the projection step, in the first iteration, the four derived images I_{00} , I_{10} , I_{01} , and I_{11} are used as the initial input to *back projection*. In other iterations, an estimation HR image $f^{(n)}$ has already been generated. It is used to form four simulated LR images. First, three shifted HR images are generated by shifting the estimation HR image by one pixel in the cross-track direction, one pixel in the along-track direction, and one pixel in both directions. Together with the estimation HR image, now, there are a total of four HR images. The four simulated LR images are then formed by down-sampling the four HR images, i.e., every 2×2 pixels in each of the four HR images are averaged and taken as a pixel of the simulated LR image. In order to overcome the possible pixel shift in the generated LR image, we compare the average value with those of the four HR pixels, take the closest pixel as the location of the new pixel, and assign the average value to this pixel. In the back-projection step, the difference images between the four simulated LR images and the four initial input images are first up sampled by expanding them into the same spatial resolution as the HR image. This is normally done by using zero-order linear interpolation or bilinear interpolation. Then, the difference images are deshifted. The improved HR image $f^{(n+1)}$ is obtained by combining all corresponding pixels of the LR images in terms of (9). In this paper, we set the iteration number to ten in order to obtain a satisfactory image quality.

IV. EXPERIMENTAL RESULTS OF SINGLE-BAND HR IMAGES

This section shows the experimental results of single-band HR images obtained using the three methods for deriving

subpixel-shifted images and two schemes of organizing the derived subpixel-shifted images described before.

A. Image Quality Metric—MVIF

Before reporting the experimental results of a single-band HR image produced using the methodology described earlier, it is necessary to define an image quality metric to measure the HR image quantitatively. The simplest and most widely used quality metric is peak signal-to-noise ratio (PSNR) that is based on the mean square error computed by averaging the squared intensity differences between the distorted and the reference image pixels. However, PSNR is not well matched to perceived visual quality [24]–[30]. Two distorted images with the same PSNR may have very different types of errors, some of which are much more visible than others. Thus, one image may look very much similar to the reference, whereas another may look very much distorted [30]. Sheikh and Bovik developed methods to measure image information based on the human visual system models [31]. They proposed to assess visual quality of a test image in terms of the amount of image information that a human brain could extract from the test image related to the amount of information that the human brain could extract from the reference image. They defined the ratio of the test image information to the reference image information as visual information fidelity (VIF)

$$\text{VIF} = \frac{\sum_{j \in \text{subbands}} I(\vec{C}^{N,j}; \vec{F}^{N,j} |_{S^{N,j}})}{\sum_{j \in \text{subbands}} I(\vec{C}^{N,j}; \vec{E}^{N,j} |_{S^{N,j}})} \quad (10)$$

where $I(\vec{C}^{N,j}; \vec{E}^{N,j} |_{S^{N,j}})$ and $I(\vec{C}^{N,j}; \vec{F}^{N,j} |_{S^{N,j}})$ represent the information volumes that could be ideally extracted by the brain from a particular wavelet subband in the test image and in the reference, respectively. For all practical distortion types, VIF lies in the interval [0, 1]. In case that the image is not distorted at all and VIF is calculated between the reference image and its copy, VIF is *exactly* unity. If the information volume of a test image is larger than that of the reference image, the VIF value is *larger* than unity. This is a distinct feature of VIF over traditional image quality assessment methods.

To the best of our knowledge, VIF is one of the best full-reference image quality metrics published in literature. That is why, it is selected to assess the image quality of the spatial-resolution-enhanced image in this paper. However, VIF requires the test image and the reference image to have the same size. In this paper, the image sizes of the spatial-resolution-enhanced image and the original image are not the same. We have proven that VIF equation (10) can be slightly modified to

$$\text{MVIF} = \frac{\sum_{j \in \text{subbands}} I(\vec{C}^{N,j}; \vec{F}^{N,j} |_{S^{N,j}})}{f_{\text{size}} \times \sum_{j \in \text{subbands}} I(\vec{C}^{N,j}; \vec{E}^{N,j} |_{S^{N,j}})} \quad (11)$$

when the sizes of the test image and the reference image are not the same and have a factor of size of f_{size} . This VIF is referred to as modified VIF (MVIF) in this paper [32].

B. Test Data Cubes

Two data cubes acquired using the airborne SFSI sensor are tested. The first testing data cube was collected for studying target detection from SWIR hyperspectral data cube with 240 bands covering a spectral range between 1224 and 2427 nm with a band center spacing of 5.2 nm. The GSD is 2.20 m \times 1.85 m. The size of the data cube is 140 lines by 496 pixels by 240 bands. Man-made targets with different materials and sizes were deployed in a mixture of sand and low-density grass covering within the scene of the data cube. Seven pieces of awnings with varying sizes ranging from 12 m \times 12 m to 0.2 m \times 0.2 m, four pieces of polythene, four pieces of white tarp, and four pieces of white cotton with varying sizes ranging from 6 m \times 6 m to 0.5 m \times 0.5 m were deployed. A green felt of size 2 m \times 2 m is deployed. In addition, a 3 m \times 3 m piece of white tarp was placed on a large vinyl turf mat of size 11 m \times 14 m. The upper part of Fig. 12 shows the layout of the man-made targets, and the lower part shows the disposition of the targets on the ground viewed in an IKONOS PAN scene with 1-m resolution. This test data cube is referred to as “target data cube” in this paper.

The second testing data cube is collected over Key Lake in northern Saskatchewan, Canada, for studying the capability of imaging spectrometers in identifying uranium mine and associated activities [9]. The data cube was acquired with the same spectral range and interval as the target data cube but with a different GSD of 3.19 m \times 3.13 m. The size of the data cube is 1090 lines by 496 pixels by 240 bands. The uranium mine site located at the Key Lake site is one of several in the Athabasca sandstone formation. Key Lake is no longer functioning as a mine. Now, the facilities at Key Lake process high-grade uranium ore trucked in from a mine at a distance of 80 km. The scene of the testing data cube includes a mill complex and a mine complex.

C. Results of Target Data Cube

Due to the target data cube acquired by the SFSI sensor being in the SWIR region, the man-made targets of size equal to or larger than 6 m \times 6 m barely showed up in the band images between 1289 and 1364 nm (from bands 13 to 28) as a result of the fact that the GSD of the data cube is 2.20 m \times 1.85 m and there is a rotational angle of approximation of 36° between the target array and the cross-track line. Fig. 13(a) shows the image of band 13 after linear contrast enhancement. According to the target layout information in Fig. 12, the targets of 12 m \times 12 m and 6 m \times 6 m awnings, 6 m \times 6 m white tarp, 6 m \times 6 m polythene, and 6 m \times 6 m cotton are barely identifiable within the red window. The 11 m \times 14 m vinyl turf mat shows up in dark outside the red window (close to the lower left corner of the window). In order to emphasize these targets, the image of band 13 is shown in Fig. 13(b) after using ENVI software tool's interactive linear histogram stretching and median filtering. It can be seen from the zoomed image that these targets are blurred out and connected to each other (except the 6 m \times 6 m white tarp).

Fig. 13(c) shows the HR image at a factor of two produced using the bicubic interpolation on the image of band 13 with the same interactive linear histogram stretching and median

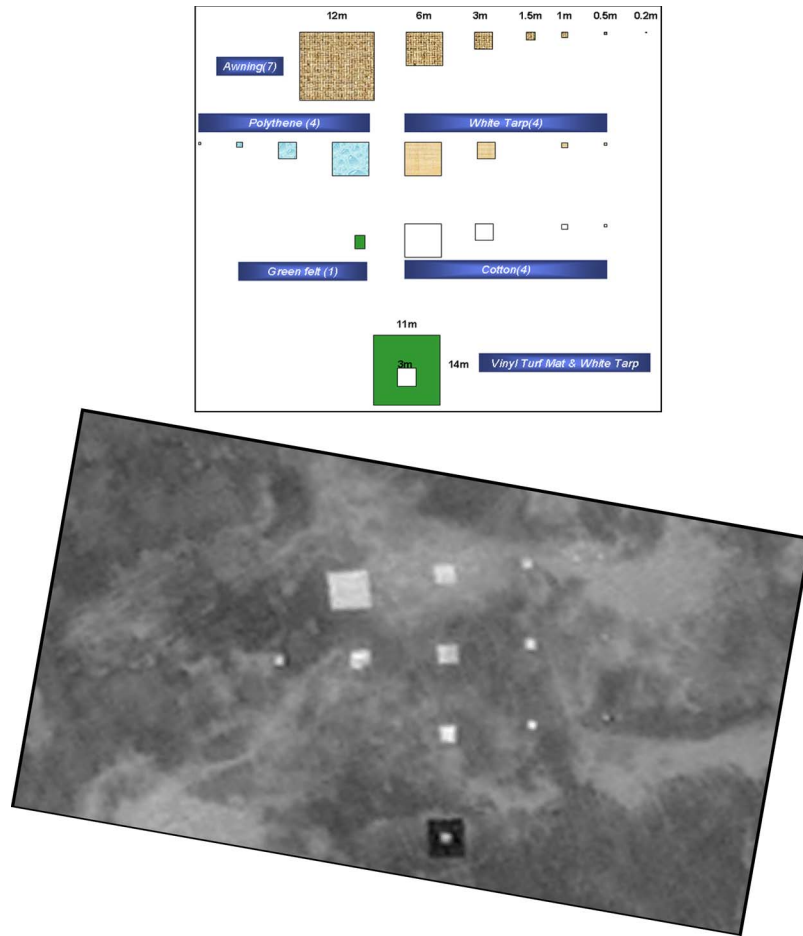


Fig. 12. (Upper part) Layout of the man-made targets of the testing data cube 1 and (lower part) the targets on the ground viewed in an IKONOS PAN scene (1-m resolution).

filtering as in Fig. 13(b). From the zoomed image, it can be seen that the targets are still blurred out and connected to each other. The only improvement is that the pixels become finer, owing to the interpolation. The MVIF of the interpolated HR image is 0.92, listed in Table I. This MVIF value indicates that this HR image produced using the interpolation does not contain more information than the original image on which it is based.

Four images were extracted from bands 13, 18, 23, and 28 of the target data cube with band 13 being taken as the baseline image. These band images were selected because the man-made targets barely showed up only in the images between band 13 and 28. The pixel shifts induced by KS among these band images are relatively small and vary in a range of 0–0.38 pixels. These four images then were arranged using two organizing schemes before being input to IBP algorithm. The IBP algorithm produced two HR images with a factor of two after a predefined ten iterations. Listed in Table I, the MVIF of the HR image with image organizing Scheme 1 is 0.99, while the MVIF of the HR image with image organizing Scheme 2 is 1.03. The MVIF greater than 1.0 indicates that, after enhancement of spatial resolution, the HR image contains more information than the original image.

Fig. 13(d) shows the HR image using image organizing Scheme 2 with the same display condition as Fig. 13(b) and (c). It is observed from the HR image that the targets are distinct

and well separated. The 12 m \times 12 m awning target even approximately outlines a square shape with one edge aligning with the direction of the target array, as shown in Fig. 13(a). The total number of pixels in the bright area is counted. It is equal to 148 pixels. Using this number of pixels, the area of the target can be estimated as follows:

$$\begin{aligned} \text{Total \# of pixels} \times \frac{\text{Area per ground pixel}}{f_{\text{size}}} \\ = 148 \times \frac{2.20 \text{ m} \times 1.85 \text{ m}}{2 \times 2} = 150.6 \text{ m}^2. \end{aligned}$$

This value is reasonably close to the real target area of 12 m \times 12 m = 144 m². The four 6 m \times 6 m targets of awning, white tarp, polythene, and cotton are relatively close to their real target areas except the 6 m \times 6 m awning target that spreads out with lower intensity. It is also observed that small awning targets (1.5 m \times 1.5 m and 1 m \times 1 m) in the HR image are better distinguishable in the cross-track direction than in the original image. This is expected as the additional spatial information induced by KS shift is in the cross-track direction. It is also noticed that the green felt can be barely seen in the HR image. This target cannot be seen in either the original image or the interpolated image.

With band 13 as the baseline image, three synthetic images with KS-induced shifts close to 0.1, 0.3, and 0.4 pixel related to

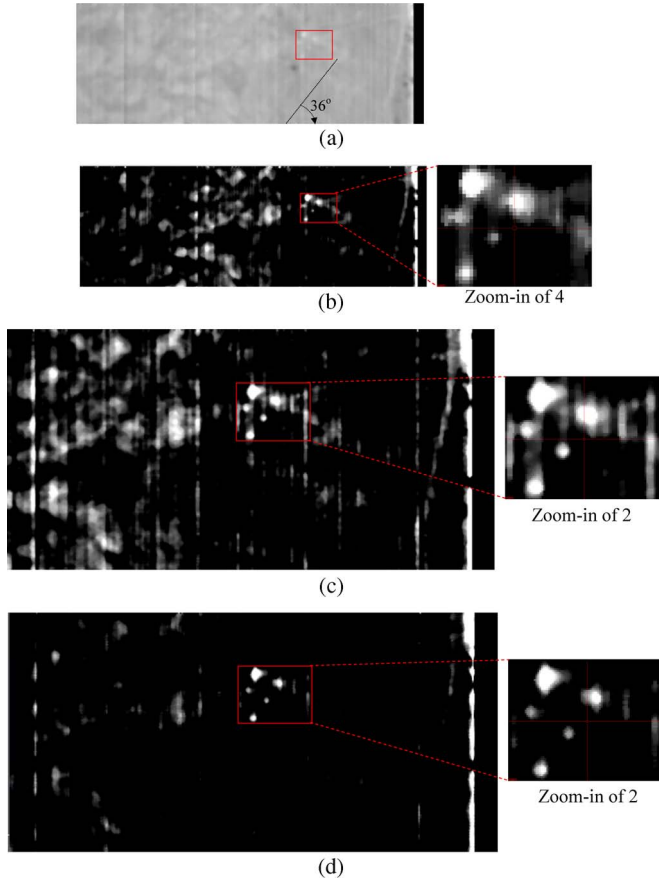


Fig. 13. Results of HR image of the man-made target data cube. (a) Band image at 1289 nm (band 13). (b) Band image after interactive histogram stretching. (c) HR image with a factor of two produced using interpolation on (a). (d) HR image with a factor of two produced using Method 1 for deriving subpixel-shifted images and image organizing Scheme 2.

TABLE I
MVIF OF THE HR IMAGES PRODUCED FROM THE TARGET DATA CUBE
USING THE PROPOSED METHODS AND TWO ORGANIZING
SCHEMES (BASELINE IMAGE: BAND 13)

Method for derived images	Modified VIF	
	Scheme 1	Scheme 2
Interpolation of baseline image	0.92	
Method 1 - Four band images extracted from the datacube	0.99	1.03
Method 2 - Synthetic images derived based on a given sub-pixel shift	1.04	1.08
Method 3 - Synthetic images derived based on closeness of pixel intensity	1.09	1.12

the baseline image were derived using Method 2 described in Section III-C. The columns that compose the synthetic images were picked up from the band images across all the spectral bands. After arrangement of the four synthetic images using the two organizing schemes, two HR images were produced using IBP algorithm. In organizing the synthetic images using Scheme 2, the synthetic image with 0.4-pixel KS-induced shift was assigned as I_{10} . The synthetic image with 0.3-pixel KS-induced shift was used for forming I_{11} , and the synthetic image with 0.1-pixel KS-induced shift was used for forming I_{01} . This is because Scheme 2 does not compensate the KS-shifted images to 1/2-pixel shift. The MVIFs of two HR images are

TABLE II
MVIF OF THE HR IMAGES PRODUCED FROM KEY LAKE DATA CUBE
USING THE PROPOSED METHODS AND TWO ORGANIZING SCHEMES

Method for derived images	Modified VIF	
	Scheme 1	Scheme 2
Interpolation of baseline image (band 65)	0.95	
Method 1 - Four band images extracted from the datacube (baseline image: band 65)	1.00	1.03
Method 2 - Synthetic images derived based on a given sub-pixel shift (baseline image: band 65)	1.01	1.04
Interpolation of baseline image (band 16)	0.93	
Method 3 - Synthetic images derived based on closeness of pixel intensity (baseline image: band 16)	1.03	1.06

1.04 and 1.08, corresponding to the two organizing schemes. The MVIFs of these two HR images are greater than those of the two HR images produced using the four band images; this is probably because the KS-induced shifts among the synthetic images are not constrained within a small number of bands and thus are relatively larger. These two HR images are not shown in this paper, since they are similar to the HR image in Fig. 13.

Three synthetic images were derived by finding the first, second, and third closest intensities of each pixel at the same location of the baseline image (band 13) using Method 3 described in Section III-D. The KS-induced shift of each pixel between the baseline image and each of the synthetic images varies as a function of pixel location in the two spatial directions (i.e., cross-track and along-track). The shift between the pixels of the baseline image and each of the three synthetic images covers a range from -0.63 to 0.58 pixels. In Scheme 2, the algorithm automatically measures the average KS-induced shifts (0.21, 0.29, and 0.36 pixel) and assigns the synthetic image with the closest to 1/2-pixel shift as I_{10} , with the second closest to 1/2-pixel shift as I_{11} . The MVIFs of two HR images produced using these synthetic images are 1.09 and 1.12, corresponding to the two organizing schemes. These MVIFs are better than those of the HR images using the other two image deriving methods. This is probably attributed to the relatively closer intensities of the pixels in the baseline image and in the synthetic images and the fact that there is no intensity normalization undertaken among the images.

It is also noticed that the MVIFs of the HR images produced using image organizing Scheme 2 are slightly better than those using image organizing Scheme 1. This is probably caused by the additional error introduced in resampling the KS-induced shifts to a uniform 1/2 pixel in Scheme 1.

D. Results of Key Lake Data Cube

Table II lists the MVIF of the HR images produced for the Key Lake data cube. The band image at 1549 nm (band 65) was taken as the baseline image for the HR images using Methods 1 and 2, and the band image at 1304 nm (band 16) was taken as the baseline image for the HR images using Method 3. The MVIFs of the HR images produced using interpolation of single-band images 65 and 16 are 0.95 and 0.93, respectively.

Four band images were extracted from bands 65, 72, 84, and 96 of the Key Lake data cube by using Method 1. These band images were selected because they locate in a spectral region with relatively higher and flatter amplitude. The range of

KS-induced pixel shift is 0–0.58 pixel among these images. The MVIFs of the HR images produced using Method 1 with the two organizing schemes are 1.00 and 1.03.

Three synthetic images with KS-induced shifts close to 0.2, 0.3, and 0.4 pixel related to the baseline image (band 65) were derived using Method 2. In organizing the synthetic images using Scheme 2, the synthetic image with 0.4-pixel shift was assigned as I_{10} . The synthetic image with 0.3-pixel shift was used for forming I_{11} , and the synthetic image with 0.2-pixel shift was used for forming I_{01} . The MVIFs of the HR images produced using Method 2 with the two organizing schemes are 1.01 and 1.04.

With band 16 as the baseline image, three synthetic images were derived using Method 3. The KS-induced shift between the pixels of the baseline image and each of the three synthetic images covers a range from -0.54 to 0.55 pixel. The MVIFs of two HR images produced using these synthetic images are 1.03 and 1.06, corresponding to the two organizing schemes. Similar to the target data cube, the MVIFs produced using Method 3 are still better than those of the HR images using the other two methods. The MVIFs of the HR images produced using organizing Scheme 2 are also slightly better than those using organizing Scheme 1.

Fig. 14 shows the original Key Lake image at 1304 nm (band 16) and the HR image produced using Method 3 with image organizing Scheme 2 after contrast enhancement using ENVI software tool's histogram equalization. In the mill complex located in the center left of the scene, there are five square-shape monitoring ponds, two reservoirs (shown only a half for the small one), processing facilities, and buildings. These objects are all displayed in dark in Fig. 14 due to the instrument wavelength range being in the SWIR region. It is observed that these objects in the HR image are more distinct. The edges of the objects are finer in the HR image than in the original image. A small region of interest (ROI) is selected (marked by a red box) and zoomed in using cubic modality with a factor of two to show the details. It can be seen that the intersection of the three roads is better separated in the HR image than in the original image. A small triangle outlined by the roads, which cannot be seen in the original image, can be barely identified in the HR image. The edge of the reservoir located in the center of the ROI is smoother in the HR image than in the original image. At the lower right corner of the ROI, there is a mining lay-down area that cannot be well identified in the original image. The outline and three rows of the lay-down area can be better identified in the HR image.

V. INCREASE SPATIAL RESOLUTION OF AN ENTIRE DATA CUBE

This section describes the enhancement of spatial resolution of an entire hyperspectral data cube using the HR image obtained by exploiting the KS-induced information of the data cube. In this paper, this HR image is used as a PAN image as in the case of the conventional spatial-resolution enhancement of hyperspectral imagery. There is no need to geometrically register the HR image with each band image of the data cube, since the HR image is derived from the data cube.

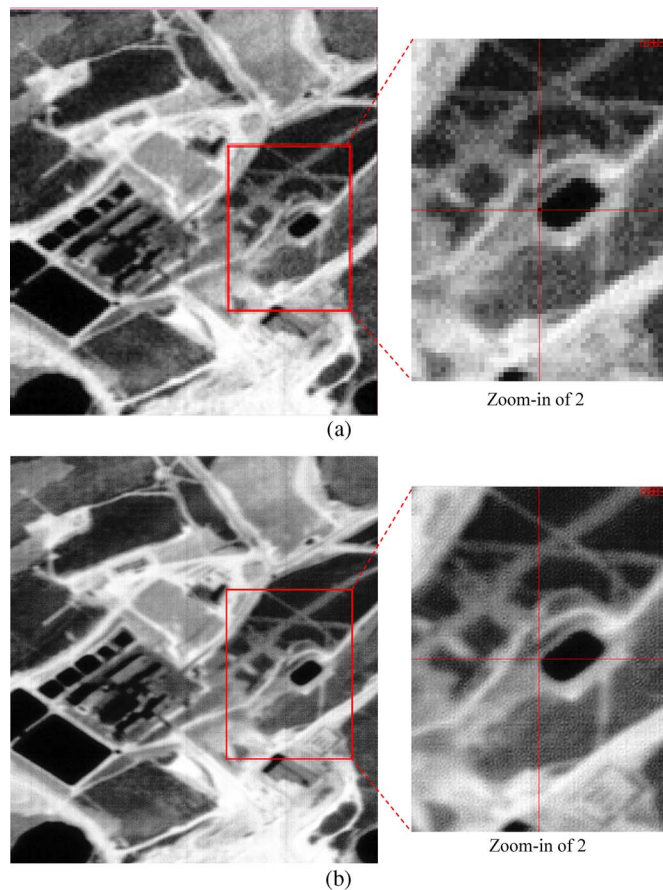


Fig. 14. Result of HR image of Key Lake data cube. (a) Band image at 1304 nm (band 16). (b) HR image with a factor of two produced using Method 3 for deriving subpixel-shifted images and image organizing Scheme 2.

Several approaches to enhancing the spatial resolution of hyperspectral data cubes have been reported. Most of them have heritage in the sharpening of multispectral imagery based on a higher resolution PAN image. These include component substitution [33]–[36], wavelet transform methods [37]–[51], least squares estimation [52], [53], statistical methods [54], linear mixing model [55]–[58], MAP estimation [59]–[62], and more recent methods [63], [65].

In this paper, a novel complex ridgelet transform (CRT)-based method [66] is utilized to fuse the HR image to each band image of the data cube for increasing the spatial resolution of the entire data cube. This method was proposed because the ridgelet transform is capable of well capturing the line and curve singularities within an image, whereas the wavelet transform is incapable of. The dual-tree complex wavelet transform (DTCWT) has the approximate shift-invariant property, which is critical for image spatial-resolution enhancement. The combination of these two transforms is referred to as the CRT and can take the advantages of both of them. The experimental results reported in [66] show that this fusion method produces much better PSNR than the fusion methods using PCA, wavelet transform, and ridgelet transform.

Fig. 15 shows the flow chart of this method. The CRT image fusion method requires that a data cube to be fused must have the same spatial size as the HR image. Each band image of the

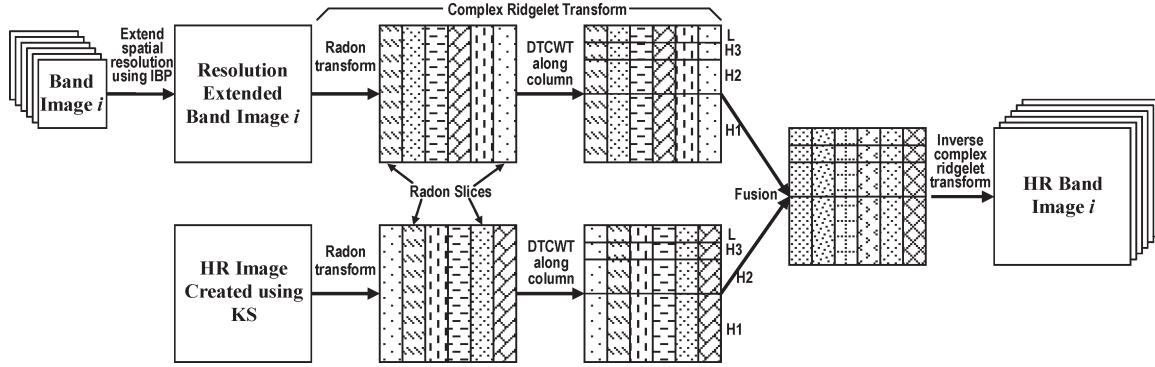


Fig. 15. Flow chart of CRT-based method for enhancing the spatial resolution of a hyperspectral data cube.

data cube needs to be extended to the same spatial grid as the HR image.

Radon transform is first applied to the HR image, and each of the grid-extended band images of the data cube to generate Radon slice images. A Radon slice is a set of Radon coefficients or a 1-D column. Then, 1-D DTCWT is applied to each of the Radon slices. In this way, the complex ridgelet coefficients have been finally generated for both the HR image and each of the band images of the data cube.

The complex ridgelet coefficients of the HR image are fused with those of each of the band images of the data cube according to the following rules:

$$c_{F,K}^L = c_{A,K}^L, \quad \text{for low-frequency coefficients} \quad (12)$$

$$c_{F,K}^H = \begin{cases} c_{A,K}^H, & \text{if } |c_{A,K}^H| \geq |c_{B,K}^H| \\ c_{B,K}^H, & \text{otherwise,} \end{cases} \quad \text{for high-frequency coefficients} \quad (13)$$

where A is the grid-extended band image, B is the HR image, F is the resolution-enhanced image, and K is the index of the complex ridgelet coefficients.

An inverse CRT is performed in order to generate the spatial-resolution-enhanced data cube.

VI. EXPERIMENTAL RESULTS OF A DATA CUBE AFTER SPATIAL-RESOLUTION ENHANCEMENT

In our experiments, the IBP is used to extend each band image of the data cube to the same spatial grid as the HR image. For a band image, three shifted images are produced by shifting the band image one pixel in the cross-track direction, one pixel in the along-track direction, and one pixel in both cross-track and along-track directions. The band image and its three shifted images are used as inputs for the IBP algorithm to generate the grid-extended image. The IBP iteration stops when a predefined difference error is reached or the maximum iteration number (e.g., ten) is reached, whatever which one comes first.

It is necessary to normalize the intensity of the HR image to that of each band image of the data cube before enhancing the spatial resolution using the CRT method, since the intensity of a band image varies with the spectral-band number.

Figs. 16 and 17 show the MVIF values of the band images of the target and Key Lake data cubes after enhancing spatial resolution using the CRT method. It should be noted that, for the

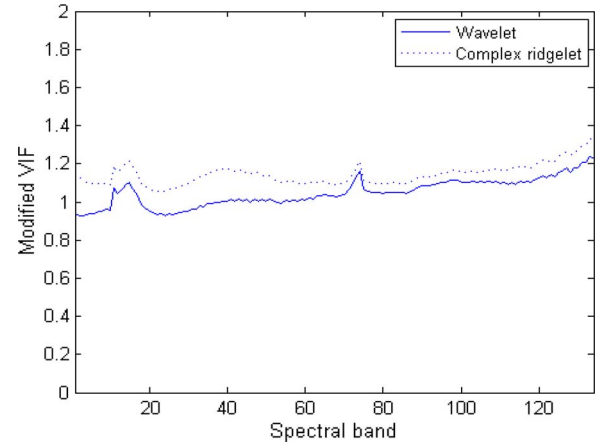


Fig. 16. MVIF values of the band images after enhancing the spatial resolution using the CRT-based method and the wavelet-based method for the target data cube.

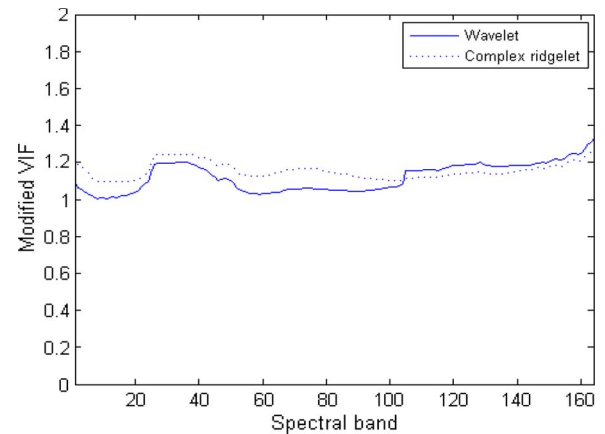


Fig. 17. MVIF values of the band images after enhancing the spatial resolution using the CRT-based method and the wavelet-based method for the Key Lake data cube.

target data cube, bands 1–5, 110–170, and 231–240 have been removed due to water absorption peaks and extremely low SNR in those bands. Similarly, for the Key Lake data cube bands 1–10, 30–50, 115–170, and 231–240 have been removed. In the figures, the MVIF values of spatial-resolution-enhanced band images using the wavelet-based method are also shown for the sake of comparison. The HR image used is the HR image produced using Method 3 (i.e., synthetic images derived based on closeness of pixel intensity) with image organizing Scheme 2,

TABLE III
OVERALL MVIF OF AN ENTIRE DATA CUBE AFTER
SPATIAL-RESOLUTION ENHANCEMENT USING THE CRT-BASED
METHOD AND THE WAVELET-BASED METHOD ON THE
TARGET AND KEY LAKE DATA CUBES

Datacube	Complex ridgelet	Wavelet
Target	1.14	1.05
Key Lake	1.15	1.12

since this HR image showed the best MVIF of single-band image in exploiting the KS characteristic. The MVIF values of the band images after spatial-resolution enhancement are improved significantly for the band images with low amplitude and poor SNR. This is because the MVIF is the ratio of the information volume of the spatial-resolution-enhanced image to the information volume of the original band image. The information volume of these spatial-resolution-enhanced images is elevated by the information from the HR image.

It can be seen from the figures that the CRT method produces better HR band images than those produced using the wavelet-transform-based method in terms of MVIF.

Table III tabulates the overall MVIF value for an entire data cube using the CRT and wavelet methods. The reason that the overall MVIF of the two spatial-resolution-enhanced data cubes is greater than the MVIF of the HR image obtained by exploiting the KS characteristic is that the MVIF of the noisy band images of the enhanced data cubes is improved significantly after fusing with the HR image, as shown in Figs. 16 and 17. The overall MVIF of the enhanced data cube is the average MVIF of all the band images after spatial-resolution enhancement.

The VIF and MVIF are to measure the information in 2-D images conveyed by the human visual system. They are limited to the evaluation of hyperspectral data cubes after enhancement of spatial resolution. We propose to use spectral angle mapper (SAM) to assess the spectral distortion of the hyperspectral data cubes after spatial-resolution enhancement. The SAM is defined as follows:

$$\text{SAM} = \cos^{-1} \left(\frac{\sum_{b=1}^{n_b} DN_O(b) \bullet DN_P(b)}{\sqrt{\sum_{b=1}^{n_b} [DN_O(b)]^2 \sum_{b=1}^{n_b} [DN_P(b)]^2}} \right) \quad (14)$$

where $DN_O(b)$ and $DN_P(b)$ are digital numbers at spectral band b of an original spectrum and the spectrum after spatial-resolution enhancement at the same location of the scene and n_b is the total number of spectral bands. SAM varies between zero and π (180°), where zero indicates a perfect match between the original and produced spectra.

Image quality metrics *Erreur Relative Globale Adimensionnelle de Synthèse* (ERGAS) [29], structural similarity (SSIM) index [30], and VIF [31] have also been used to evaluate the image sequences of the hyperspectral data cubes after spatial-resolution enhancement. The ERGAS is defined as

$$\text{ERGAS} = 100 \frac{d_h}{d_l} \sqrt{\frac{1}{L} \sum_{l=1}^L \left(\frac{\text{rmse}(l)}{\mu(l)} \right)^2} \quad (15)$$

TABLE IV
SAM, ERGAS, MSSIM, AND VIF OF DATA CUBES AFTER
SPATIAL-RESOLUTION ENHANCEMENT USING THE CRT-BASED METHOD
AND THE WAVELET-BASED METHOD ON THE DOWN-SAMPLED TARGET
AND KEY LAKE DATA CUBES (WITH A FACTOR OF TWO)

Datacube	Metrics	Complex Ridgelet	Wavelet
Target	SAM	1.37°	2.84°
	ERGAS	4.91	7.47
	MSSIM	0.99	0.92
	VIF	0.98	0.92
Key Lake	SAM	2.25°	3.81°
	ERGAS	5.68	6.63
	MSSIM	0.96	0.73
	VIF	1.06	0.99

where d_h/d_l is the ratio between pixel sizes of the HR image and an LR band image, $\mu(l)$ is the mean of the l th band, and L is the total number of bands. This index measures a distortion and thus must be as small as possible.

The SSIM index compares local correlations in luminance, contrast, and structure between the reference and test images. The SSIM index is defined as

$$\text{SSIM}(x, y) = \frac{\sigma_{xy} + C_1}{\sigma_x \sigma_y + C_1} \cdot \frac{2\mu_x \mu_y + C_2}{\mu_x^2 + \mu_y^2 + C_2} \cdot \frac{2\sigma_x \sigma_y + C_3}{\sigma_x^2 + \sigma_y^2 + C_3} \quad (16)$$

where μ_x , μ_y , σ_x^2 , σ_y^2 , and σ_{xy} are the same as in (15). The constants C_1 , C_2 , and C_3 stabilize SSIM when the means and variances become small. The best value of SSIM is 1.0 if $x = y$ for all pixels. The mean SSIM (MSSIM) over the whole image gives the final quality measure.

It is known that the SAM, ERGAS, SSIM, and VIF are all full-reference metrics. This means that the size of a test data cube and the size of the reference data cube should be the same. In this paper, after spatial-resolution enhancement, the size of the enhanced data cube is larger than the size of the original data cube. The large-size original data cube does not exist. In order to use these metrics, we propose to down-sample the original hyperspectral data cubes first and then apply the KS-based spatial-resolution-enhancement approaches to the down-sampled data cubes to produce spatial-resolution-enhanced data cubes. In this way, the data cubes after spatial-resolution enhancement have the same size as the original data cubes.

It is worth mentioning that the evaluation results obtained by assessing the proposed spatial-resolution-enhancement approaches on the down-sampled data cubes may not reflect the real performance of the KS-based approaches. This is because the down-sampling process may alter the characteristics of the spectral pixels of the instrument that acquired the hyperspectral data cubes and may compromise the ability of KS characteristics for enhancing spatial resolution.

The target and Key Lake data cubes were down sampled by a factor of two in our experiments. The same processes that were applied to the original target and Key Lake data cubes as in Table III were applied to the down-sampled data cubes. Table IV lists the evaluation results of SAM, ERGAS, MSSIM, and VIF by comparing the enhanced data cubes with the original data cubes. The values listed in the table are the overall (i.e., average) values of all the spectral bands of the data cubes.

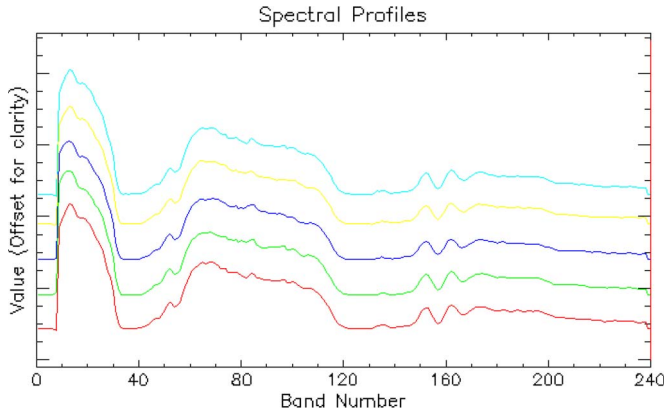


Fig. 18. Example of (red) spectral curve of the awning material extracted from the original data cube and (green, blue, yellow, and light blue) spectral curves of the 2×2 pixels in the HR grid extracted from the target data cube after spatial-resolution enhancement using CRT.

It can be seen from the table that the overall SAMs between the original data cubes and the enhanced data cubes are all very small. For the target data cube, the overall SAM values are 1.37° and 2.84° , respectively, corresponding to the enhanced data cube by using CRT- and wavelet-based methods. The overall SAM values are 2.25° and 3.81° , respectively, for the Key Lake data cube. These small SAM values indicate that the spectra of the enhanced data cubes are very close to those of the original data cubes. Fig. 18 shows an example of spectral curve of a pixel extracted from the original data cube (red) and spectral curves of the produced 2×2 pixels (green, blue, yellow, and light blue) extracted from the target data cube after spatial-resolution enhancement using CRT. This pixel is the purest pixel of the awning material in the target data cube, whose location has been identified in [67].

The overall ERGAS values are 4.91 and 5.68 for the target and Key Lake data cubes produced using the CRT. The overall ERGAS values for both data cubes produced using the wavelet are 7.47 and 6.63.

The overall MSSIM values for both data cubes produced using the CRT are 0.99 and 0.96, which are very close to 1.0. The overall MSSIM values for both data cubes produced using the wavelet method are 0.92 and 0.73.

The overall VIF values for the target and Key Lake data cubes produced using the CRT are 0.98 and 1.06, respectively, which are smaller than the MVIF values listed in Table III. This result is consistent with our concern mentioned before that assessing the proposed KS-based spatial-resolution-enhancement approaches by applying it on the down-sampled data cubes may compromise the ability of KS characteristics for enhancing the spatial resolution. The overall VIF values for the target and Key Lake data cubes produced using the wavelet method are 0.92 and 0.99, respectively, which are also worse than those in Table III.

A comprehensive assessment of the spectral information distortion after the spatial-resolution enhancement currently is ongoing that uses remote sensing applications as measures in collaboration with our active hyperspectral user community. We will report the assessment results when the new results are available.

VII. CONCLUSION

This paper has developed a novel two-step technology that can enhance the spatial resolution of a hyperspectral data cube without using any additional images, as would be the case in image fusion. In the first step, the technology exploits interband spatial misregistration or distortion (often referred to as “KS”) of the sensor that acquired the data cube and uses it as additional information to create a single-band HR image. Then, in the second step, the single-band HR image is used to enhance the spatial resolution in the cross-track direction of each band image of an entire data cube.

In creating the single-band HR image by exploiting the sensor’s intrinsic KS characteristics, three methods have been developed to derive subpixel-shifted images from the data cube itself. Two schemes were proposed to organize the derived subpixel-shifted images before being integrated into the HR image using the IBP fusion. Method 1 is the simplest of the three methods, which extracts subpixel-shifted images from the original band images of the data cube. The subpixel shifts of such derived images related to the baseline image span a range. Method 2 derives synthetic images at a column-by-column basis with all pixels having very close subpixel shifts related to the baseline image. The intensity normalization of the synthetic images has less impact, as it is done column by column, instead of the normalization of an entire image as in Method 1. Method 3 derives synthetic images in a way that the intensities of the pixels are close to those of the baseline image. Thus, the pixel intensities of the synthetic images do not need to be normalized. This may reduce the impact of intensity normalization on the quality of the single spatial-resolution image. Image organizing Scheme 2 produces slightly better MVIFs of the single-band HR images than using image organizing Scheme 1.

A CRT-based method was utilized to fuse the created high-spatial-resolution image to each band image of the data cube. The IBP was adopted to extend each band image of the data cube to the same spatial grid as the single-band HR image. For the sake of comparison, the widely used wavelet-based image fusion method was also tested. Experimental results show that the proposed two-step technology can increase the spatial resolution of hyperspectral data cubes by a factor of two.

VIII. FUTURE WORK

We will consider the following research works in the future.

We will study the most recent contributions in the superresolution and replace IBP with these new methods. We know that the strengths of IBP are the ease of learning and implementation, while its weaknesses are that this method does not have unique solution due to the ill-posed nature of the inverse problem and it has some difficulty in choosing the back-projection kernel. This kernel is very critical because it determines the contribution of the error properly, i.e., it determines how the error between real and estimated LR images affects the new estimate of the HR image and, as a consequence, its choice affects the characteristics of the solution where there are possible solutions. We think that a linear interpolation without iterations would be also effective and could save time. For this aim, a nearest neighbor kernel is evidently unsuitable.

We will study the diversity of spectral features in different bands of a hyperspectral data cube, which could be a very critical issue in exploiting KS distortion on the entire data cube. It may be evident that the HR image could not be derived by considering bands belonging to different regions of the spectrum or near the absorption peak wavelengths, because the spectral features that these bands recognize could unfit each other and produce an HR image where the noise is dominant.

A good alternative quality index at full resolution, particularly for hyperspectral data cubes, is to measure the SAM index between fused and up-sampled band images. This SAM index is not fully optimal because the derived HR band images are slightly different from the up-sampled band images, but it is a good indicator particularly to assess that the spectral features have not been heavily altered by the procedure.

ACKNOWLEDGMENT

The authors would like to thank R. Neville of the Canada Centre for Remote Sensing (retired) for providing the KS information of the SFSI sensor and test data cubes and J. Lévesque of the Defence Research and Development of Canada for providing the test data cubes.

REFERENCES

- [1] A. Hollinger, M. Bergeron, M. Maszkiewicz, S.-E. Qian, H. Othman, K. Staenz, R. A. Neville, and D. G. Goodenough, "Recent developments in the Hyperspectral Environment and Resource Observer (HERO) mission," in *Proc. IGARSS*, Jul. 2006, pp. 1620–1623.
- [2] C. Pohl and J. L. Van Genderen, "Multisensor image fusion in remote sensing: Concept, methods and applications," *Int. J. Remote Sens.*, vol. 19, no. 5, pp. 823–854, 1998.
- [3] P. R. Coppin and M. E. Bauer, "Digital change detection in forest ecosystems with remote sensing imagery," *Remote Sens. Rev.*, vol. 13, pp. 207–234, 1996.
- [4] D. P. Roy, "The impact of misregistration upon composited wide field of view satellite data and implications for change detection," *IEEE Trans. Geosci. Remote Sens.*, vol. 38, no. 4, pp. 2017–2032, Jul. 2000.
- [5] I. Zavorin and J. Le Moigne, "Use of multiresolution wavelet feature pyramids for automatic registration of multisensor imagery," *IEEE Trans. Image Process.*, vol. 14, no. 6, pp. 770–782, Jun. 2005.
- [6] R. A. Neville, L. Sun, and K. Staenz, "Detection of keystone in image spectrometer data," *Proc. SPIE*, vol. 5425, pp. 208–217, 2004.
- [7] K. Staenz, T. Szeredi, and J. Schwarz, "ISDAS—A system for processing/analyzing hyperspectral data," *Can. J. Remote Sens.*, vol. 24, no. 2, pp. 99–113, 1998.
- [8] R. A. Neville, N. Rowlands, R. Marois, and I. Powell, "SFSI: Canada's first airborne SWIR imaging spectrometer," *Can. J. Remote Sens.*, vol. 21, no. 3, pp. 328–336, 1995.
- [9] R. A. Neville, K. Staenz, J. Levesque, C. Nadeau, O. S. Truong, and G. A. Borstad, "Uranium mine detection using an airborne imaging spectrometer," in *Proc. 5th Int. Airborne Remote Sens. Conf.*, San Francisco, CA, Sep. 17–20, 2001.
- [10] S. C. Park, M. K. Park, and M. G. Kang, "Super-resolution image reconstruction: A technical overview," *IEEE Signal Process. Mag.*, vol. 20, no. 3, pp. 21–36, May 2003.
- [11] J. L. Brown, "Multi-channel sampling of low pass signals," *IEEE Trans. Circuits Syst.*, vol. CAS-28, no. 2, pp. 101–106, Feb. 1981.
- [12] J. J. Clark, M. R. Palmer, and P. D. Laurence, "A transformation method for the reconstruction of functions from nonuniformly spaced samples," *IEEE Trans. Acoust., Speech, Signal Process.*, vol. ASSP-33, no. 5, pp. 1151–1165, Oct. 1985.
- [13] S. P. Kim and N. K. Bose, "Reconstruction of 2-D band limited discrete signals from nonuniform samples," in *Proc. Inst. Elec. Eng. F—Radar Signal Process.*, Jun. 1990, vol. 137, no. 3, pp. 197–204.
- [14] R. Y. Tsai and T. S. Huang, "Multipleframe image restoration and registration," in *Advances in Computer Vision and Image Processing*. Greenwich, CT: JAI Press, 1984, pp. 317–339.
- [15] A. K. Katsaggelos, *Digital Image Restoration*. Heidelberg, Germany: Springer-Verlag, 1991.
- [16] P. Cheeseman, B. Kanefsky, R. Kraft, J. Stutz, and R. Hanson, "Super-Resolved Surface Reconstruction From Multiple Images," NASA Ames Res. Center, Moffett Field, CA, Tech. Rep. FIA-94-12, Dec. 1994.
- [17] B. C. Tom and A. K. Katsaggelos, "Reconstruction of a high-resolution image by simultaneous registration, restoration, and interpolation of low-resolution images," in *Proc. IEEE Int. Conf. Image Process.*, Washington, DC, Oct. 1995, vol. 2, pp. 539–542.
- [18] R. R. Schulz and R. L. Stevenson, "Extraction of high-resolution frames from video sequences," *IEEE Trans. Image Process.*, vol. 5, no. 6, pp. 996–1011, Jun. 1996.
- [19] R. C. Hardie, K. J. Barnard, and E. E. Armstrong, "Joint MAP registration and high-resolution image estimation using a sequence of undersampled images," *IEEE Trans. Image Process.*, vol. 6, no. 12, pp. 1621–1633, Dec. 1997.
- [20] H. Stark and P. Oskoui, "High resolution image recovery from image-plane arrays, using convex projections," *J. Opt. Soc. Amer. A*, vol. 6, no. 11, pp. 1715–1726, Nov. 1989.
- [21] A. M. Tekalp, M. K. Ozkan, and M. I. Sezan, "High-resolution image reconstruction from lower-resolution image sequences and space varying image restoration," in *Proc. IEEE ICASSP*, San Francisco, CA, Mar. 1992, vol. 3, pp. 169–172.
- [22] M. Irani and S. Peleg, "Improving resolution by image registration," *CVGIP: Graph. Models Image Process.*, vol. 53, no. 3, pp. 231–239, May 1991.
- [23] M. Irani and S. Peleg, "Motion analysis for image enhancement resolution, occlusion, and transparency," *J. Vis. Commun. Image Represent.*, vol. 4, no. 4, pp. 324–335, Dec. 1993.
- [24] B. Girod, "What's wrong with mean-squared error," in *Digital Images and Human Vision*, A. B. Watson, Ed. Cambridge, MA: MIT Press, 1993, pp. 207–220.
- [25] P. C. Teo and D. J. Heeger, "Perceptual image distortion," in *Proc. SPIE*, 1994, vol. 2179, pp. 127–141.
- [26] A. M. Eskicioglu and P. S. Fisher, "Image quality measures and their performance," *IEEE Trans. Commun.*, vol. 43, no. 12, pp. 2959–2965, Dec. 1995.
- [27] M. P. Eckert and A. P. Bradley, "Perceptual quality metrics applied to still image compression," *Signal Process.*, vol. 70, no. 3, pp. 177–200, Nov. 1998.
- [28] S. Winkler, "A perceptual distortion metric for digital color video," in *Proc. SPIE*, 1999, vol. 3644, pp. 175–184.
- [29] T. Ranchin and L. Wald, "Fusion of high spatial resolution and spectral resolution images: The ARSIS concept and its implementation," *Photogramm. Eng. Remote Sens.*, vol. 66, no. 1, pp. 49–61, Jan. 2000.
- [30] Z. Wang, A. C. Bovik, H. R. Sheikh, and E. P. Simoncelli, "Image quality assessment: From error visibility to structural similarity," *IEEE Trans. Image Process.*, vol. 13, no. 4, pp. 600–612, Apr. 2004.
- [31] R. H. Sheikh and A. C. Bovik, "Image information and visual quality," *IEEE Trans. Image Process.*, vol. 15, no. 2, pp. 430–444, Feb. 2006.
- [32] S.-E. Qian and G. Chen, "Four reduced-reference metrics for measuring hyperspectral images after spatial resolution enhancement," in *Proc. IAPRS*, vol. 37, *ISPRS TC VII Symposium—100 Years ISPRS*, W. Wagner and B. Székely, Eds., Vienna, Austria, Jul. 2010, pp. 204–208.
- [33] W. J. Carper, T. M. Lillesand, and R. W. Kiefer, "The use of intensity–hue–saturation transformations for merging SPOT panchromatic and multispectral image data," *Photogramm. Eng. Remote Sens.*, vol. 56, p. 459–46, 1990.
- [34] M. Gonzalez-Audicana, X. Otazu, O. Fors, and J. Alvarez-Mozos, "A low computational-cost method to fuse IKONOS images using the spectral response function of its sensors," *IEEE Trans. Geosci. Remote Sens.*, vol. 44, no. 6, pp. 1683–1691, Jun. 2006.
- [35] M. Choi, "A new intensity–hue–saturation fusion approach to image fusion with a tradeoff parameter," *IEEE Trans. Geosci. Remote Sens.*, vol. 44, no. 6, pp. 1672–1682, Jun. 2006.
- [36] V. K. Shettigara, "A generalized component substitution technique for spatial enhancement of multispectral images using a higher resolution data set," *Photogramm. Eng. Remote Sens.*, vol. 58, no. 5, pp. 561–567, 1992.
- [37] D. P. Filberti, S. E. Marsh, and R. A. Schowengardt, "Synthesis of imagery from high spatial and spectral resolution from multiple image sources," *Opt. Eng.*, vol. 33, no. 8, pp. 2520–2528, Aug. 1994.
- [38] L. Peytavin, "Cross-sensor resolution enhancement of hyperspectral images using wavelet decomposition," in *Proc. SPIE*, 1996, vol. 2758, pp. 193–203.
- [39] R. B. Gomez, A. Jazaeri, and M. Kafatos, "Wavelet-based hyperspectral and multispectral image fusion," in *Proc. SPIE*, Apr. 2001, vol. 4383, pp. 36–42.

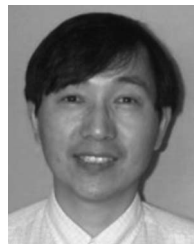
- [40] Y. Zhang and M. He, "Multispectral and hyperspectral image fusion using 3D wavelet transform," *J. Electron. (China)*, vol. 24, no. 2, pp. 218–224, Mar. 2007.
- [41] D. G. Jun, Z. Haifang, and Z. Chaojie, "Hyperspectral resolution enhancement using high-resolution imagery with wavelet package algorithm and optimal index principle," in *Proc. Int. Archives Photogramm., Remote Sens. Spatial Inf. Sci.*, Beijing, China, 2008, vol. 37, pp. 1223–1226, Part B7.
- [42] G. Hong and Y. Zhang, "Comparison and improvement of wavelet-based image fusion," *Int. J. Remote Sens.*, vol. 29, no. 3, pp. 673–692, Feb. 2008.
- [43] B. Aiazzi, L. Alparone, S. Baronti, and A. Garzelli, "Context driven fusion of high spatial and spectral resolution images based on oversampled multiresolution analysis," *IEEE Trans. Geosci. Remote Sens.*, vol. 40, no. 10, pp. 2300–2312, Oct. 2002.
- [44] S. Li, J. K. Kwok, and Y. Wang, "Using the discrete wavelet frame transform to merge Landsat TM and SPOT panchromatic images," *Inf. Fusion*, vol. 3, no. 1, pp. 17–23, Mar. 2002.
- [45] Y. Chibani and A. Houacine, "The joint use of IHS transform and redundant wavelet decomposition for fusing multispectral and panchromatic images," *Int. J. Remote Sens.*, vol. 23, no. 18, pp. 3821–3833, Sep. 2002.
- [46] Y. Chibani and A. Houacine, "Redundant versus orthogonal wavelet decomposition for multisensor image fusion," *Pattern Recognit.*, vol. 36, no. 4, pp. 879–887, Apr. 2003.
- [47] M. Gonzalez-Audiciana, J. L. Saleta, and R. G. Catalan, "Fusion of multispectral and panchromatic images using improved IHS and PCA mergers based on wavelet decomposition," *IEEE Trans. Geosci. Remote Sens.*, vol. 42, no. 6, pp. 1291–1299, Jun. 2004.
- [48] G. Pajares and J. M. de la Cruz, "A wavelet-based image fusion tutorial," *Pattern Recognit.*, vol. 37, no. 9, pp. 1855–1872, Sep. 2004.
- [49] M. González-Audiciana, X. Otazu, O. Fors, and A. Seco, "Comparison between Mallat's and the "à trous" discrete wavelet transform based algorithms for the fusion of multispectral and panchromatic images," *Int. J. Remote Sens.*, vol. 26, no. 3, pp. 595–614, Feb. 2005.
- [50] T. Ranchin and L. Wald, "Fusion of high spatial and spectral resolution images: The ARSIS concept and its implementation," *Photogramm. Eng. Remote Sens.*, vol. 66, no. 1, pp. 49–61, 2000.
- [51] A. E. Iverson and J. R. Lersch, "Adaptive image sharpening using multiresolution representations," in *Proc. SPIE*, 1994, vol. 2231, pp. 72–83.
- [52] J. C. Price, "Combining panchromatic and multispectral imagery from dual resolution satellite instruments," *Remote Sens. Environ.*, vol. 21, no. 2, pp. 119–128, Mar. 1987.
- [53] C. K. Munechika, J. S. Warnick, C. Salvaggio, and J. R. Schott, "Resolution enhancement of multispectral image data to improve classification accuracy," *Photogramm. Eng. Remote Sens.*, vol. 59, pp. 67–72, 1993.
- [54] R. Nishii, S. Kusanobu, and S. Tanaka, "Enhancement of low resolution image based on high resolution bands," *IEEE Trans. Geosci. Remote Sens.*, vol. 34, no. 5, pp. 1151–1158, Sep. 1996.
- [55] G. D. Robinson, H. N. Gross, and J. R. Schott, "Evaluation of two applications of spectral mixing models to image fusion," *Remote Sens. Environ.*, vol. 71, no. 3, pp. 272–281, Mar. 2000.
- [56] H. N. Gross and J. R. Schott, "Application of spectral mixture analysis and image fusion techniques for image sharpening," *Remote Sens. Environ.*, vol. 63, no. 2, pp. 85–94, Feb. 1998.
- [57] M. E. Winter and E. M. Winter, "Physics-based resolution enhancement of hyperspectral data," in *Proc. SPIE*, 2002, vol. 4725, pp. 580–587.
- [58] N. Keshava and J. F. Mustard, "Spectral unmixing," *IEEE Signal Process. Mag.*, vol. 19, no. 1, pp. 44–57, Jan. 2002.
- [59] R. C. Hardie and M. T. Eismann, "MAP estimation for hyperspectral image resolution enhancement using an auxiliary sensor," *IEEE Trans. Image Process.*, vol. 13, no. 9, pp. 1174–1184, Sep. 2004.
- [60] M. T. Eismann and R. C. Hardie, "Resolution enhancement of hyperspectral imagery using coincident panchromatic imagery and a stochastic mixing model," in *Proc. IEEE Workshop on Advances in Techniques for Analysis of Remotely Sensed Data*, Oct. 27/28, 2003, vol. 6361, pp. 282–289, DOI: 10.1109/WARSD.2003.1295206.
- [61] M. T. Eismann and R. C. Hardie, "Application of the stochastic mixing model to hyperspectral resolution enhancement," *IEEE Trans. Geosci. Remote Sens.*, vol. 42, no. 9, pp. 1924–1933, Sep. 2004.
- [62] M. T. Eismann and R. C. Hardie, "Hyperspectral resolution enhancement using high-resolution multispectral imagery with arbitrary response functions," *IEEE Trans. Geosci. Remote Sens.*, vol. 43, no. 3, pp. 455–465, Mar. 2005.
- [63] C. L. Hsu, P. Y. Tu, and C. H. Lee, "An adjustable pan-sharpening approach for IKONOS/QuickBird/GeoEye-1/WorldView-2 imagery," *IEEE J. Sel. Topics Appl. Earth Obs. Remote Sens.*, vol. 5, no. 1, pp. 125–134, Feb. 2012.
- [64] S. Li, "A new pan-sharpening method using a compressed sensing technique," *IEEE Trans. Geosci. Remote Sens.*, vol. 49, no. 2, pp. 738–746, Feb. 2011.
- [65] S. Rahmani, M. Strait, D. Merkurjev, M. Moeller, and T. Wittman, "An adaptive IHS pan-sharpening method," *IEEE Geosci. Remote Sens. Lett.*, vol. 7, no. 4, pp. 746–750, Oct. 2010.
- [66] G. Chen, S.-E. Qian, and J.-P. Ardouin, "Superresolution of hyperspectral imagery using complex ridgelet transform," *Int. J. Wavelets, Multiresolution Inf. Process.*, vol. 10, no. 3, 2012.
- [67] S.-E. Qian, H. Othman, and J. Lévesque, "Spectral angle mapper based assessment of detectability of man-made targets from hyperspectral imagery after SNR enhancement," in *Proc. SPIE*, Sep. 2006, vol. 6361, pp. 63611H-1–63611H-8.



Shen-En Qian (M'97–SM'03) received the B.Eng. degree in industrial electrical automation from the Hefei University of Technology, Hefei, China, in 1982, the M.S. degree in optoelectronics from the Chinese Academy of Sciences, Beijing, China, in 1985, and the Ph.D. degree in communication and electronic systems from Jilin University, Changchun, China, in 1990.

From 1985 to 1993, he was a Professor with the Changchun Institute of Optics and Fine Mechanics, Chinese Academy of Sciences, Changchun, and he was with the Département de Recherche Spatiale, Observatoire de Paris-Meudon, Centre National de la Recherche Scientifique, Paris, France, for one and a half years. Since January 1995, he has been with the Canadian Space Agency, St-Hubert, QC, Canada, where he is currently a Senior Research Scientist. He is the scientific authority of Canadian government contracts in the development of space technologies and satellite missions. He is the Head of an R&D team in the development of space technology and spaceborne electro-optical instruments and their applications for remote sensing. He is the holder of eight U.S. patents, three European patents, and several pending patents. He is an author or coauthor of three books and over 100 scientific papers in the areas of spaceborne optical sensors, satellite sensor data enhancement, compression, processing and analysis, Earth observation applications, data handling systems of spacecraft payloads, space data and information systems, hyperspectral imagery, remote sensing, optoelectronic signal detection and reception, weak-signal detection, and intelligent instrumentation.

Dr. Qian is a Fellow of the Society of Photo-Optical Instrumentation Engineers. He was the recipient of the Marie Curie Award (European Community International Scientific Cooperation Program) in 1992. He was twice the recipient of the Director Award of Federal Government of Canada in 1999 and 2002 for his outstanding contribution to R&D in space technology and satellite mission within the government facility. He was also the recipient of the Award of Canadian Government Invention in 2004 for his multiple patents for satellite missions.



Guangyi Chen received the B.Sc. in Applied Mathematics from Dalian University of Technology, Dalian, China, in 1986, the M.Sc. in Computing Mathematics from Chinese Academy of Sciences, China, Shenyang, in 1989, the second M.Sc. in Computer Science from Concordia University, Montreal, Canada, in 1999, and the Ph.D. in Computer Science from Concordia University, Montreal, Canada, in 2004. During his graduate and postdoctoral studies, he was awarded a visiting fellowship in the Canadian Government Laboratories, a Natural Sciences and Engineering Research Council of Canada (NSERC) postdoctoral fellowship, a Canadian Space Agency Postdoctoral Fellowship Supplement, an NSERC PGS B Fellowship, an FCAR Scholarship, the J. W. McConnell Memorial Graduate Fellowship, and the Concordia University External Award Holder Doctoral Fellowship.

He is currently with the Canadian Space Agency, Saint-Hubert, QC, Canada. He is currently an Editor for the *International Journal of Applied Mathematics and Statistics*. His research interests include pattern recognition, signal/image/video processing, machine learning, artificial intelligence, and scientific computing.